Article:
Banfi, E.G., Sala, E.M., Gajjela, R.S.R. et al. (2025) An atomically resolved study of droplet epitaxy InAs quantum dots grown on InGa(As,P)/InP by MOVPE for quantum photonic applications. Journal of Applied Physics, 137 (13). 134401. ISSN: 0021-8979

https://doi.org/10.1063/5.0232155

Journal of Applied Physics

RESEARCH ARTICLE | APRIL 02 2025

An atomically resolved study of droplet epitaxy InAs quantum dots grown on InGa(As,P)/InP by MOVPE for quantum photonic applications

E. G. Banfi ; E. M. Sala ; R. S. R. Gajjela ; J. Heffernan ; P. M. Koenraad

J. Appl. Phys. 137, 134401 (2025)
https://doi.org/10.1063/5.0232155

Journal of Applied Physics ARTICLE pubs.aip.org/aip/jap

An atomically resolved study of droplet epitaxy InAs quantum dots grown on InGa(As,P)/InP by MOVPE for quantum photonic applications

Cite as: J. Appl. Phys. **137**, 134401 (2025); doi: 10.1063/5.0232155
Submitted: 5 August 2024 · Accepted: 10 March 2025 ·
Published Online: 2 April 2025

E. G. Banfi,[1,a)] E. M. Sala,[2] R. S. R. Gajjela,[1] J. Heffernan,[2] and P. M. Koenraad[1]

AFFILIATIONS

[1]Department of Applied Physics and Science Education, Eindhoven University of Technology, Eindhoven 5612 AZ, The Netherlands
[2]EPSRC National Epitaxy Facility and Department of Electronic and Electrical Engineering, Sheffield S37HQ, United Kingdom

[a)]**Author to whom correspondence should be addressed:** e.g.banfi@tue.nl

ABSTRACT

We investigated droplet epitaxy InAs/InP quantum dots (QDs) grown by MOVPE on two different substrate interlayers of InGaAs and InGaAsP, both lattice-matched to InP, by cross-sectional scanning tunneling microscopy (X-STM) and AFM (atomic force microscopy). We compared, at the atomic scale, the structural and compositional properties of the QDs grown on the two different surfaces. On both interlayers, the QDs present a truncated pyramid shape with a rhomboid base, flat top and bottom facets, and side planes corresponding to {136} planes. Finite element simulations (FESs) are performed to fit the experimental outward relaxation of the QDs and the lattice constant profiles. The X-STM results and FES confirm that the QDs grown on InGaAsP present a composition with less than 5% P intermixing, whereas the QDs on InGaAs have a slightly higher P incorporation but still less than 10% of P intermixing. This study confirms that both interlayers suppress the etching mechanisms, previously identified as etch pits and trenches, when growing InAs QDs directly on InP. The InGaAs and InGaAsP interlayers both show lateral composition modulation, with much stronger fluctuations and filamentation displayed in the InGaAsP interlayer. We demonstrate that the growth on InGaAsP produces InAs QDs with a high crystal quality comparable to those grown on InP and control over the etching mechanisms. The detailed study performed in this work shows the successful integration of high-quality InAs/InP QDs with the InGaAsP surface, which is used in many applications in a wide range of photonic devices and quantum technologies.

I. INTRODUCTION

Ever since their discovery in the early 1980s, semiconductor quantum dots (QDs) have demonstrated an interesting range of applications. Originally rooted in the exploration of organic photochemistry,[1] semiconductor quantum dots have now diversified their applications significantly. These include serving as the active medium for lasers,[2,3] playing a crucial role in quantum information technologies,[4–7] as building blocks for memory devices,[8,9] as semiconductor optical amplifiers (SOA),[10] and being utilized in display technologies.[11] The future of QDs is even more promising, with new applications ranging from harvesting solar power[12] to medical treatment[13] and quantum computing.[14] Therefore, research on these nanoscale objects has been intense in the last couple of decades, and their relevance is now widely recognized in the field.

In this work, we will focus on III–V InAs QDs grown on two different interlayers of InGaAs and InGaAsP on InP substrates. The interlayer is a 5 nm tall spacer grown between the InP substrate and the QD region. Introducing an InGaAs interlayer removed etching mechanisms present when directly growing droplet epitaxy (DE) InAs QDs on InP.[15] The InGaAsP platform has been widely used as a waveguide material, and it is well-established as the material of choice for telecommunication lasers in the C-band.[10,16,17] Meanwhile, InAs/InP QDs have attracted interest as candidates for single-photon emitters due to their emission at 1.55 μm, which is the wavelength preferred for quantum

telecommunication applications due to the minimal losses of 0.2 dB/km in optical fibers.[5,18] In particular, InAs/InP QDs grown by droplet epitaxy (DE) were employed in the first Quantum Light Emitting Diode (QLED)[5,7] and demonstrated quantum teleportation of qubits and longer coherence times compared to Stranski–Krastanov (SK) QDs.[19] Moreover, the Purcell enhancement of single-photons at the C-band emitted by InAs DE QDs grown on InGaAsP/InP has recently been demonstrated.[20] Thus, the fabrication of high-quality single-photon emitters around 1.55 μm is in high demand. In this work, InAs/InP QDs grown by DE in a metal–organic vapor-phase epitaxy reactor (MOVPE) were studied. We previously demonstrated the DE growth of such QDs both on bare InP[21,22] and on interlayers lattice-matched to InP.[23,24] DE QDs offer an interesting alternative to SK QDs, particularly for quantum communication technology applications. QDs grown by DE show high symmetry and compositional homogeneity, reduced fine-structure splitting (FSS), and longer coherence times, the latter due to the wetting layer tunability, a property specifically related to DE QDs.[7,15,19] The combination of a large-scale growth technique for semiconductor materials, such as MOVPE, and the versatility of DE presents a novel and promising approach, with great potential for a technology transfer from academic research to industry. We previously explored the morphology and growth dynamics of such DE QDs at the atomic scale, both on bare InP and on an InGaAs interlayer (IL).[15,25] In our studies, we discovered that the InGaAs IL inhibited the formation of etch pits and trenches, which were observed when growing QDs directly on InP.[15,21] In this study, we characterized how, at the atomic scale, the introduction of P in the IL, which thus becomes InGaAsP, affected the morphological properties and composition of such structures. We also determined the effect of P on the occurrence of the etching, and we shed light on the QD structure and growth dynamics. The results of this study provide valuable feedback to the epitaxial growth and input for device modelers for lasers, SOA, or any other photonic or quantum telecom device working in the 1.55 μm C-band with QDs.

II. METHODS

We studied two samples with, in total, three regions of interest. Simplified models are shown in Fig. 1. Both samples, ILP (interlayer phosphorous) and ILR1/2 (interlayer reference), were grown on InP (001) wafers. Between the two samples, the main difference lies in the composition of the interlayer (IL) on which the QDs were formed. In one wafer, ILR1/2, the ILs were composed of $In_{0.53}Ga_{0.47}As$, while in the other sample, ILP, the IL was composed of $In_{0.719}Ga_{0.281}As_{0.608}P_{0.392}$. Both compositions are lattice-matched to InP. Both samples were grown in the same MOVPE reactor under similar conditions. As in our previous works,[23,24] the group V precursor materials used are arsine (AsH_3) and phosphine (PH_3) and for group III trymethylindium (TMIn) and trymethylgallium (TMGa). For both samples, the indium flow rate was 1.4 μmol min^{-1} and the droplet deposition temperature was 400 °C with a crystallization temperature of 520 °C. In the ILR1/2, the two layers had, respectively, 25 and 35 s of In deposition time. In the ILP sample, the In deposition time was 65 s. For all three regions of interest, the QDs were capped by 20 nm of InP grown at 520 °C and 80 nm of InP grown at 610 °C. For further details on the growth sequence, we refer the reader to our previous works.[23,24]

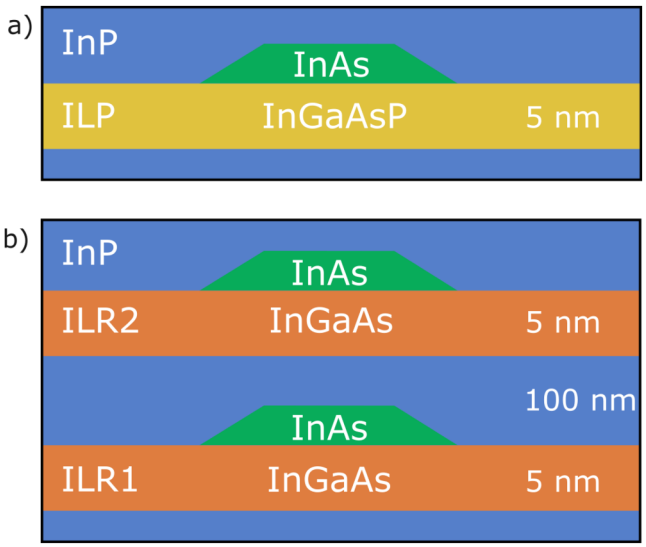

FIG. 1. Simplified sketch model (not to scale) of the two samples, ILP in (a) and ILR1 and ILR2 in (b). The different colors in the sketch correspond with the different materials. Blue represents InP, green is the InAs QD material, and ocher and orange are the interlayers, respectively, of InGaAsP and InGaAs.

To assess the morphology and crystallization of the free-standing uncapped surface QDs, the samples have been initially characterized by atomic force microscopy (AFM) right after growth. The samples studied by AFM had an additional layer of surface QDs grown under the same conditions but on top of the 100 nm thick InP burying layer. The InP layer was grown thick enough to release the stress from the QD area and avoid QD seeding onto the AFM studied layer. This characterization was carried out *ex situ* in a Bruker Dimension Icon machine by using the PeakForce tapping mode with an ultrasharp SNL-10 (sharpened silicon) tip with a radius of 2 nm and a low spring constant of 0.35 N/m. The same tip was used to perform the measurements, and no wear off of the tip was observed. The observed QD features are consistently reproducible across different samples.

To study the capped QDs at the atomic scale, cross-sectional scanning tunneling microscopy (X-STM) measurements have been conducted using a commercial Scienta Omicron Low-Temperature scanning tunneling microscope (STM) for the experiments reported in this paper. Before cooling, the pressure in the system was reduced to ultrahigh vacuum (UHV) at $4 - 6 \times 10^{-11}$ mbar by an ion-getter pump and a turbo pump. During the STM measurements performed at 77 K, liquid nitrogen temperature (LNT), the turbo was switched off and pressure was kept in this range by the ion-getter pump and cryogenic pumping. The system is equipped with two cryogenic reservoirs that are suspended in the UHV of the main STM vacuum chamber, and these offer a very large surface area at cryogenic temperatures that acts as a cold pump. This surface area is much larger than the sample area (about

150 μm by 4 mm) ensuring that the sample surface remains extremely clean during the experiments that may take up to several days. If any surface contamination occurs, this is easily recognizable as it would lead to surface adatoms that have a characteristic signature in the STM images. We are, thus, sure that our sample surface is clean during the measurements.

The samples for X-STM were prepared from a 2-in. wafer and cut into rectangles with dimensions of $4 \times 8\,\text{mm}^2$. Contacts were deposited on these samples to enhance conductivity between the sample and the holder. Afterward, they were clamped into the special sample holders and loaded into the STM setup. Prior to the measurement, samples were baked in a separate chamber at 180 °C to remove any residual water and contaminants. Subsequently, the samples were cooled down to LNT and cleaved just before the measurement to reveal one of the {110} surfaces, which are the natural cleaving planes for zincblende crystals. The combination of UHV and LNT conditions in our system allowed us to maintain the sample surface free of contaminants during the entire measurements.

The STM tips used in the current experiments were made in-house by electrochemical etching of polycrystalline W wires using a 2 M KOH solution. The tips were baked in the STM prep chamber at 230 °C to remove contaminants and were subjected to Ar sputtering to remove oxide scale and to sharpen the tip radius.

In order to get a deeper insight into the local composition of the studied QDs, X-STM measurements were compared with finite element simulations (FESs) by modeling the surface outward relaxation of the cleaved QDs due to local compressive strain. The FES executed in this work was conducted using COMSOL Multiphysics 5.6 software with the solid mechanics package.

III. RESULTS AND DISCUSSION

In our previous studies, we performed X-STM characterization of DE QDs grown by MOVPE on bare InP and InGaAs IL.[15,25] In these experiments, we learned that the direct growth of the QDs on bare InP induces the formation of etch pits underneath the QDs or trenches around the base of the QDs, depending on the growth conditions. These effects were ascribed to surface liquefaction, destabilization, and elemental migration[15] on the InP surface. Both effects strongly depend on the crystallization temperature. Etching is more likely to happen for crystallization temperatures below 500 °C and trenching above this threshold temperature. The etching processes were previously suppressed by using the InGaAs IL. The suppression is due to changes in the surface chemistry, which changes the surface diffusion of the elements, reducing the etching mechanisms. However, the growth of QDs on a InGaAs IL resulted in QDs with a lower level of purity when compared to the growth on InP. In this study, we examine the effect of introducing additional P in the IL (i.e., the InGaAsP layer), and assess the growth dynamics, e.g., formation of etch pits and/or trenches, morphological and compositional changes in the QDs. The InGaAsP framework is relevant in a number of photonic devices working in the 1.55 μm wavelength region. The ILP sample was already the subject of a recent publication by Sala *et al.*,[24] which focused on the growth, characterization, and photoluminescence (PL) spectroscopy of InAs DE QDs grown on the InGaAsP IL. There, the authors explored the effect of the different In droplet deposition temperatures and compared their nucleation on three different surfaces: InGaAsP, InGaAs, and InP. They conclude that the surface composition strongly affects the In surface diffusion and thus the droplet nucleation and QD formation. It was also hypothesized that, for an InGaAsP surface during the crystallization phase of the droplets (arsenic exposure), the IL surface becomes As-terminated due to an As–P exchange. This led to proposing a QD nucleation process similar to the growth on InGaAs.[24] They also observed on InGaAsP a much higher QD density, compared to the initial In droplet density.[24] Finally, the PL studies showed QD ensemble emission at room temperature and bright single-dot emission at low temperatures.

In the present work, we focus on the detailed structural and compositional characterization of the QDs, including IL and capping layer by AFM and X-STM to understand the growth dynamics and provide detailed feedback to further optimize the QD growth. The pairing of AFM and X-STM enables examination of the size, shape, and composition of QDs pre- and post-capping. Our findings demonstrate that growth on InGaAsP yields InAs QDs with structural and compositional qualities akin to those grown directly on InP, while also offering control over etching mechanisms and integration with the InGaAsP platform.

A. AFM characterization

From the AFM characterization of ILR1/2 and ILP shown in Fig. 2, we can gain insights into several aspects of the uncapped QDs. In both samples, ILP in Figs. 2(a) and 2(b), and ILR1 and 2 in Figs. 2(c) and 2(d), the QDs tend to exhibit an elongated shape along the horizontal direction $\{\bar{1}10\}$, and no quantum dashes are observed.[27] A significant difference in the QD density between ILP, ILR1, and ILR2 cases is observed. This is well explained by the variation in In deposition times for the three layers (see Sec. II). The histograms presented in Figs. 2(e) and 2(f) show the results of the grain analysis conducted with the Gwyddion software. Grain analysis allows the study of parameters, such as the distribution of the major and minor axes, the orientation of the elongation direction, and the surface area occupied by the QDs. For an easier comparison, the three histograms are plotted together (ILP and ILR1/2). Figure 2(e) shows that the three distributions are peaking at similar lengths of the major axis. The inset in Fig. 2(e) shows the distribution of the QD surface area. The area of the three distributions increases for an increasing amount of In deposited on the surface prior to the QD crystallization. In Fig. 2(f), we observe a similar distribution for ILR1 and 2, whereas ILP seems to have a longer minor axis on average. The inset in Fig. 2(f) shows the distribution of the angle of the major axis of the QDs with the $[\bar{1}10]$. In all the graphs in Figs. 2(e) and 2(f), the histograms for ILP, ILR1, and ILR2 are similar to each other with minor differences that can be attributed to the amount of In deposited prior crystallization. All samples show an approximate aspect ratio of 1.8 in the QD axes lengths. The axes aspect ratio plays a role in the linear density of the QDs that will be found either at the {110} or $\{\bar{1}10\}$ cleaved surfaces. When counting, in Fig. 2(b), the number of intersected QDs

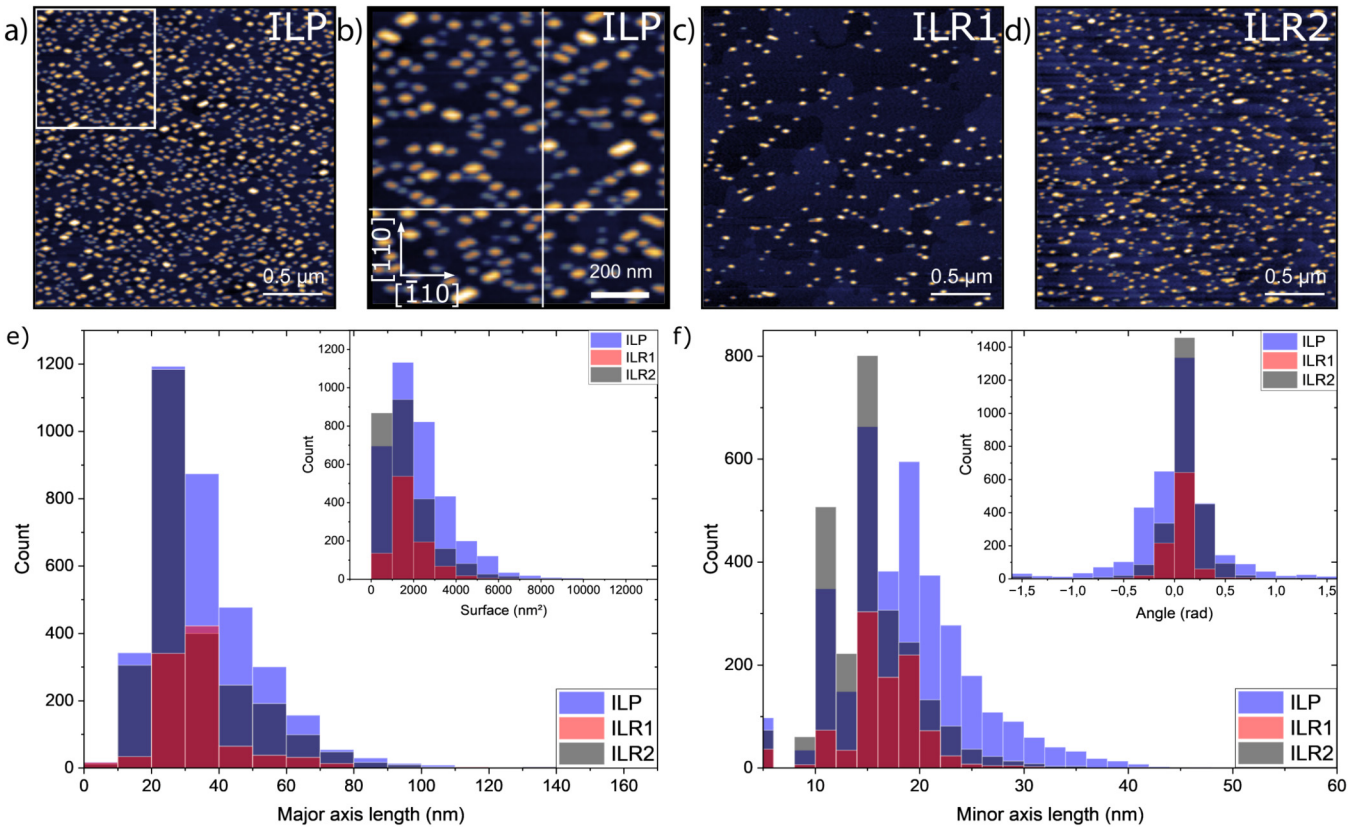

FIG. 2. (a) $2.5 \times 2.5\,\mu m^2$ AFM image of InAs DE QDs from the sample with the InGaAsP IL. The white inlaid square represents where the image in (b) was taken from; (b) $1 \times 1\,\mu m^2$ detail from (a). The white lines help the eye to count the number of QDs along each of the two natural cleaving plane directions. The two cleaving plane directions indicated here are based on Ref. 26, where it is shown that the QDs tend to be more elongated along the [1̄10]; (c) $2.5 \times 2.5\,\mu m^2$ AFM image of InAs DE QDs from the sample with IL ILR1; and (d) $2.5 \times 2.5\,\mu m^2$ AFM image of InAs DE QDs from the sample with IL ILR2. (c) and (d) differ in the amount of In that was deposited onto the surface. (d) had a 10 s longer deposition time. (e) and (f) show, respectively, the major and minor axes distributions of the QDs present in the AFM images (a), (c), and (d); the three histograms are overlapped for better comparison. The major axis is oriented along the [1̄10] direction, and the minor is perpendicular to it. The inset of (e) shows the surface area distribution of QDs. The inset of (f) shows the major axis angle distribution, where 0 is the horizontal direction.

along the vertical [110] (QDs minor axis) white line, we typically find 16 QDs, whereas along the horizontal [1̄10] (QDs major axis) line, about 10 QDs are observed. The orientation-dependent linear density will be used to determine the cleavage direction in the two X-STM measurements. We conclude from this study that there is no major effect on the QDs' shape or orientation due to the presence of P in the IL when compared to ILR1 and ILR2. When comparing our results to the growth on InP,[15] we notice that the QDs here present a rhomboid base with clear elongation along the [1̄10] direction; meanwhile, the growth on InP gave rise to nearly square-based dots. This could be due to a difference in the indium adatom surface diffusion on the different surfaces.

AFM can provide valuable information on uncapped QDs; however, the QDs must be embedded for any functionalization. QDs undergo significant changes during the capping process, including, but not limited to, compositional changes, demolition of apex, and alteration of QD size and shape.[28,29] X-STM characterizes both morphological and compositional changes in buried QDs as detailed in Sec. III B.

B. X-STM characterization

We report here the results of our X-STM study on the samples ILP and ILR1/2. Both measurements have been carried out in the same setup in UHV at LNT.

X-STM topographic images at constant current, such as the ones reported in this paper, Figs. 3, 4 and 7, mix electronic and topographic information in their contrast. It is possible to reduce the electronic contribution by measuring with a large bias between the tip and sample.[30] Therefore, we used biases from −2 V to −3 V in order to tunnel deep in the Valence Band (VB). With the suppression of the electronic contribution, our X-STM images hold information mainly related to the topography of the surface; therefore, we can reliably study the composition, size, and shape of the

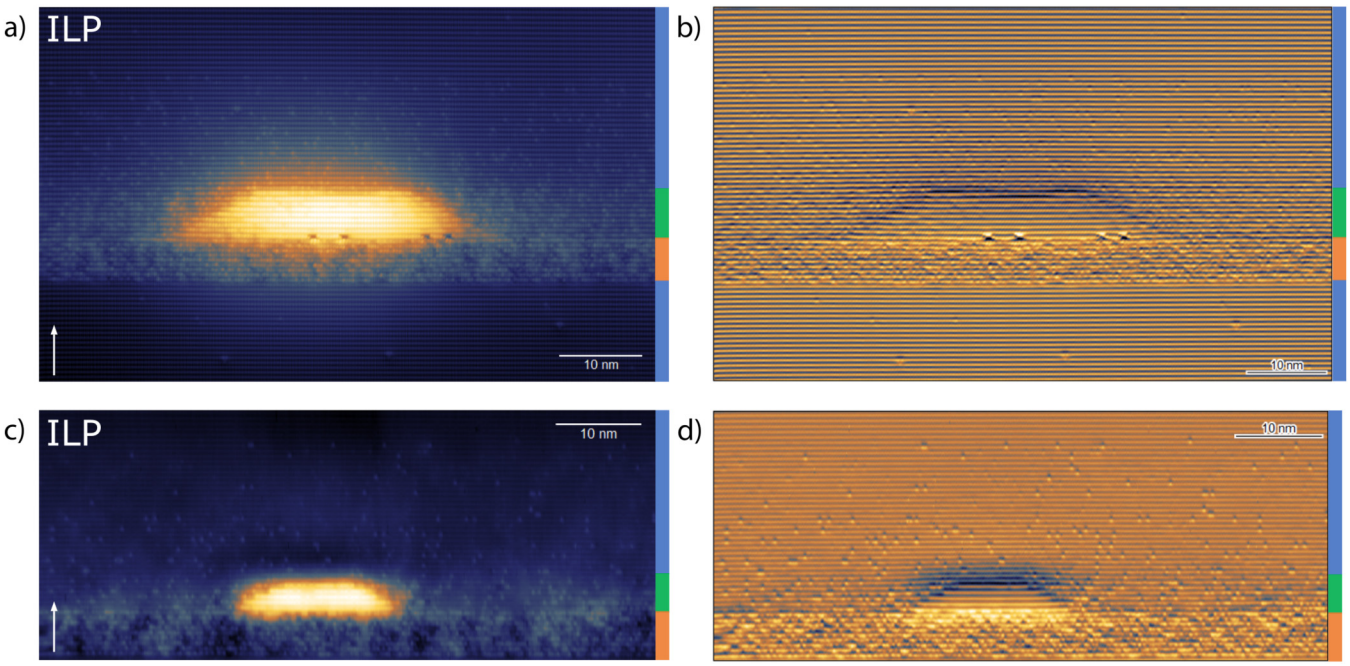

FIG. 3. Images of two InAs QDs formed on an InGaAsP IL: (a) 75 × 46 nm^2 filled state image, taken at −2 V and 100 pA, the contrast ranges from 0 (dark) to 375 pm (bright), and the white arrow indicates the growth direction [001]. The colored bars on the right-hand side of each figure help to identify the layers, and light blue at the bottom and top shows the InP regions, orange is the IL, and green shows the QD area; (b) current image of QD in (a). The current image allows us to resolve the details in the IL below the QD and away from it. (c) 72 × 29 nm^2 filled state image taken at −1.9 V and 50 pAm, and the white arrow indicates the growth direction [001]. The contrast range (from dark to bright) is 0–270 pm; (d) current image of (c).

QDs.[30] Composition fluctuations will appear both in the contrast inside the QD core and in the outward relaxation of the cleaved QD, although to interpret the relaxation data, we will require to perform FES.

When performing an X-STM measurement on the {110} planes of zincblende III–V semiconductors, we can choose which sublattice to image by applying a negative bias for group V (filled states) or a positive bias for group III (empty states).[30]

1. InGaAsP interlayer ILP

In Figs. 3(a) and 3(c), filled state topography images of two QDs from sample ILP are shown. The bright areas in the middle of the images correspond to the QDs, cleaved at random positions. The region immediately underneath the QDs, with a non-uniform contrast, is the IL region. The IL region is about 5 nm or 9/10 bilayers thick along the growth axis and is composed of InGaAsP as expected from the QD growth. Underneath the IL region, the InP buffer layer is found. The first 20 nm of InP above the QDs is grown at the same temperature as the crystallization temperature of the QDs, i.e., 520 °C, while the final InP burying layer is grown at 610 °C. The QD in Fig. 3(a) has a base length of 40 ± 1 nm, a top length of 20 ± 1 nm, and a height of 5.7 ± 0.5 nm (or 10 bilayers), whereas the QD in (c) has a base length of 18 ± 1 nm, a top length of 9 ± 1 nm, and a height of 3.1 ± 0.5 nm (or five bilayers). In both cases and for any other QDs in the ILP sample, no etch pits or trenches are observed. The QDs have a trapezoidal shape with flat top and bottom bases and sharp side facets. The angle between the base plane and the side facets of the QDs is about 27 ± 3°, which is compatible with side facets along the {136} plane.[31] Inside the QD area of Fig. 3(a), a uniform core of the QD is observed, with some minor contrast variations mostly at the edges. Figure 3(b) shows the corresponding current image of Fig. 3(a). Current images, taken simultaneously to topography, are useful for resolving local compositional variations and atomic segregation. Since the height regulation of the STM tip is not instantaneous, the current image can be interpreted as the spatial derivative of the topographic image. Therefore, contrast contributions, such as the long ranged outward relaxation of the QD area, are not as strongly present, and small local changes, such as a different atomic species, create a larger effect on the contrast[30] in the current image. In Fig. 3(a), the major contrast variations are at the bottom center and the bottom right part of the QD. These are missing atoms, pulled out of the surface during the cleaving process. These features are clearly distinguishable from longer ranged compositional variations. In Fig. 3(c), we show topography and (d) current images of a smaller QD cross section. Similar conclusions as for the previous QD can be drawn, although due to the smaller size, the internal compositional fluctuations seem to be absent. Both current images [Figs. 3(b) and 3(d)] allow for a high-resolution study of the composition of the

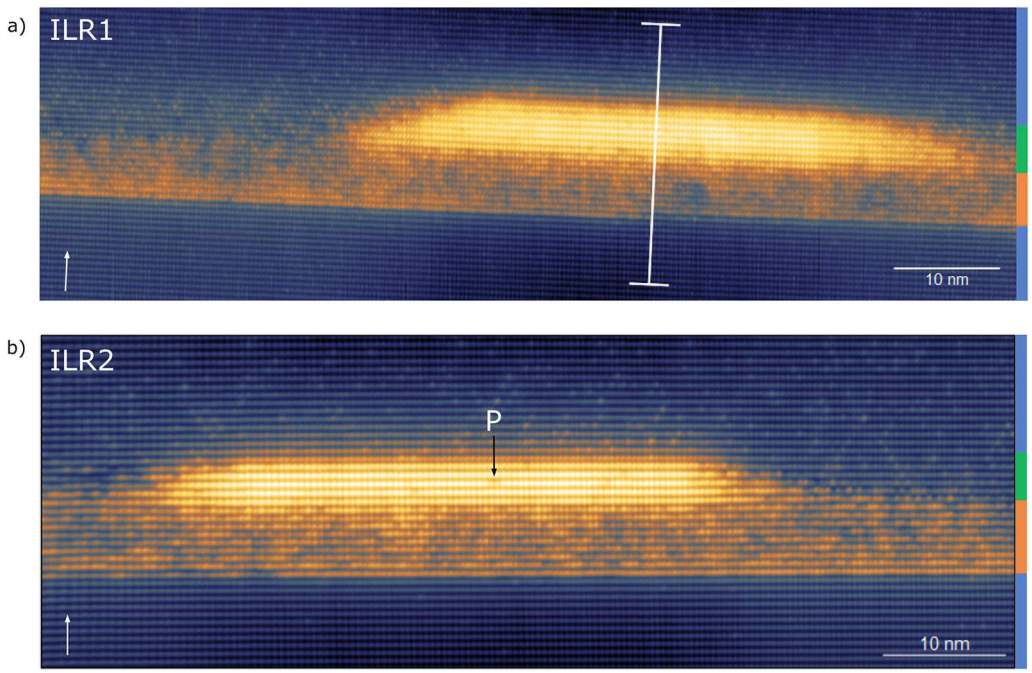

FIG. 4. (a) 92 × 27 nm^2 filled state X-STM image of InAs QD on ILR1 IL, taken at −3 V and 100 pA; the white arrow indicates the growth direction [001]. The QD has a base length of 58 ± 1 nm, a top length of 32 ± 1 nm, and a height of 5.2 ± 0.3 nm or 9 bilayers. The white line represents the position where the line profile reported in Fig. 6(c) was taken, and the tick width at the end of the line represents the area that was used to average the curve. (b) Filled state X-STM image, taken at −3 V and 100 pA, of InAs QD on ILR2; the white arrow indicates the growth direction [001]. The QD is 41 ± 1 nm in base length, 24 ± 1 in top length, and 3.1 ± 0.5 nm in height or 6 bilayers. The black arrow indicates a contrast variation due to a P atom incorporated into the QD core.

IL (InGaAsP) underneath the QDs, and in both cases, small composition fluctuations can be observed. The figure in (b) shows both InP layers above and below the QD region and the As segregation happening in the region above the QD. While a detailed analysis of As segregation was not conducted, visual inspection reveals that the arsenic segregation in the images of sample ILP is similar to that observed in the images of samples ILR1/2.

Studying the X-STM measurements of a large number of QDs cleaved at random various positions gives us an understanding of the QD three-dimensional shape, for example, by using the height vs base length distribution of the QDs.[30] For the III–V semiconductor family with a zincblende crystal structure, the {110} is the natural cleaving plane family. We can check with X-STM along which of the two planes we are measuring, as shown in Ref. 32, by performing a bias switch mid-image (in the supplementary material). For the ILP measurement, the cleave exposed the (110) plane, corresponding with the vertical direction in Fig. 2(b). The cleavage orientation plays a role in the number of QDs that will be exposed as the linear density of the QDs is not equal along the [110] or the [$\bar{1}$10]. In our X-STM experiment, we counted 14 QDs along a 1 μm line, similar to the density along the vertical line in Fig. 2(b). We conclude that in the ILP case, the QDs are cleaved parallel to the minor axis direction.

In the paper published by Sala *et al.*[24] one of the open questions was whether the reintroduction of P in the IL region underneath the QDs yields etch pits, trenches, or lateral compositional fluctuations. With this study, we show that the QDs from the ILP sample do not show etch pits underneath or trenches on either side of the QDs. Lateral composition modulation (LCM) does not seem to be related to QD nucleation; however, it is present and will also be studied in this work.

2. InGaAs interlayer ILR1/2

In order to understand the effect of P, we used sample ILR1/2 as a reference sample, which was fabricated with the same growth conditions as ILP, but with a P-free IL region. The sample has two QD layers, which were formed with different amounts of In deposited for QD growth, which will be referred to as ILR1 and ILR2 (see Sec. II).

Figure 4(a) shows a filled state (−3 V) X-STM topography image of ILR1. The QD is the bright contrast area in the middle of the figure, the area underneath the QD is the InGaAs IL, which is about 5 nm thick, and below the IL region, the InP buffer layer is found. About 100 nm of InP above ILR1 (see Sec. II), the second IL region, ILR2, is present and one of its QD is shown in Fig. 4(b). Focusing on Fig. 4(a), the QD shows parallel top and bottom bases corresponding to a section through a truncated pyramid shape.[30] The angle between the side facet and the bottom base is of 16 ± 3°, compatible with the {136} plane.[31] The ILR2 QD is the bright area in the center of Fig. 4(b), and it also has parallel top

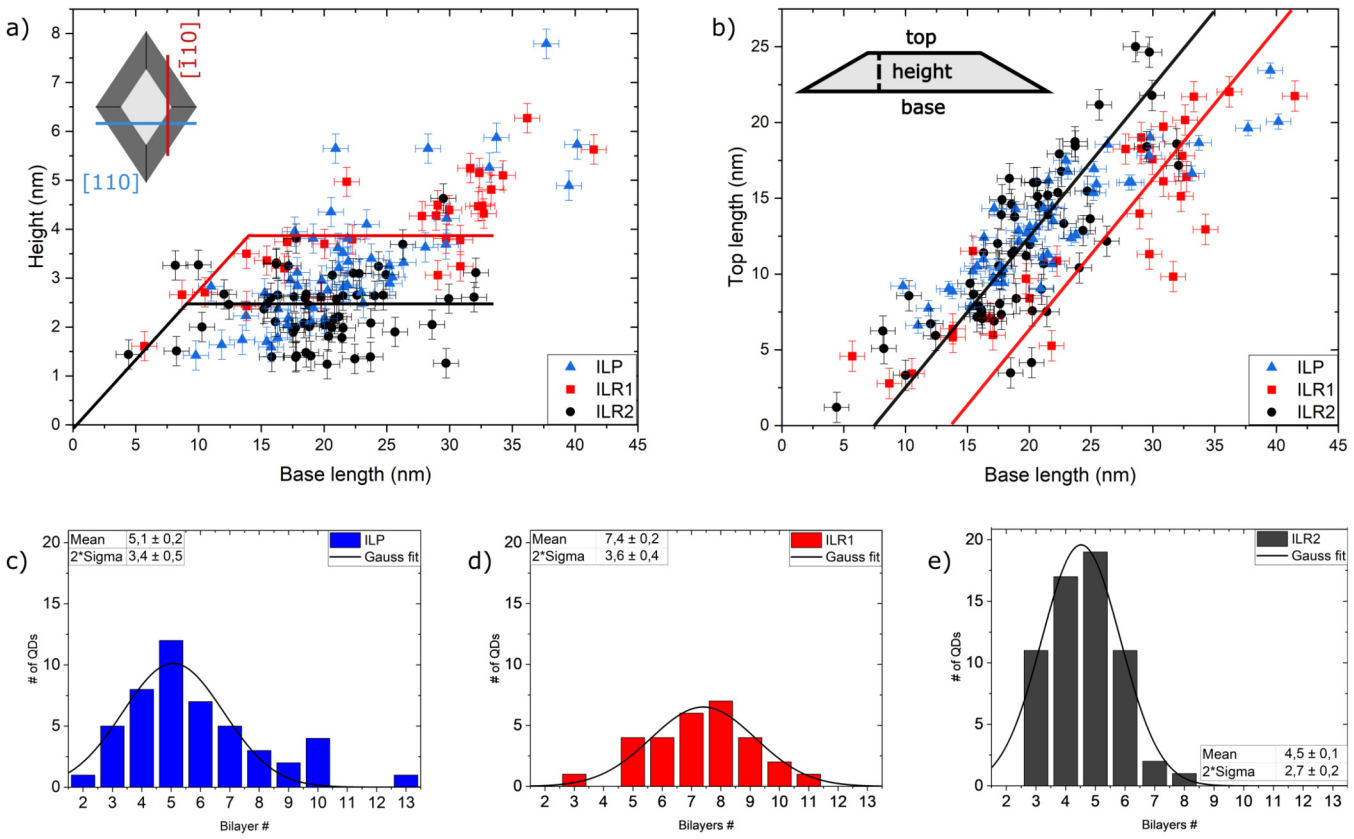

FIG. 5. (a) The QD 3D model projection in the inset in the top left corner shows the cleavage directions through the QD. ILP cleaved perpendicular to the longer axis (light blue line), while ILR1/2 cleaved perpendicular to the short axis (red line). The graph in (a) represents the relationship between the QD height and the base length. The black and red lines are intended to lead the eye through the data points. (b) The inset shows the cross section of a QD exposing the height, top, and base length. The graph shows the relationship between the QD top length and the base length for the three samples studied. The black and red lines show the linear trend in the data for samples ILR2/ILP and ILR1, respectively. (c)–(e) are the distributions of the QD height in bilayers per different sample.

and bottom bases with an angle between the lateral facets and the bottom base of about $16 \pm 3^{\circ}$ similar to the one reported in (a). During our measurement, we observed a total of 29 QDs for ILR1 and 62 QDs for ILR2. For ILR2, we could observe 11 QDs over a $3\,\mu$m line, and in the same region for ILR1, we encountered three QDs and this density is compatible with a cleave exposing the $(\bar{1}10)$ plane. The two QDs of Fig. 4, as well as all the others observed on this sample, have very similar features, and no major differences appear between the two layers (ILR1 and ILR2) except their density, which is explained by the different amount of In deposited during growth. All QDs in the samples show neither etch pits nor trenches.

3. Statistical study of the QDs measured by X-STM

We performed a statistical study of the QDs on InGaAsP and InGaAs measured by X-STM to follow up on the AFM results and to check whether InP overgrowth during capping affected the QD characteristics. Due to the nature of the cleaving process in X-STM, it is impossible to know precisely where the cleave will propagate, whether it will perfectly intersect the center of a quantum dot or only partially as shown in the inset of Fig. 5(a). When performing the statistical study of the X-STM results, taking into account the random position of the cleave through the QDs allows us to understand the approximate shape of the QD in 3D.[33]

The statistical results of the X-STM measurements are shown in Fig. 5. In Fig. 5(a), the height against the base length of each observed QD is plotted. Due to the different cleaving direction for the two samples and the clear asymmetry of the QDs [the inset of Fig. 5(a)], the data of ILR1/2 were corrected by a normalizing factor obtained from the AFM analysis from the ratio of the major and minor axis (1.8). All the data in Figs. 5(a) and 5(b) are as if the sample ILR1/2 cleavage happened along the horizontal light blue line [inset Fig. 5(a)] as in the ILP case.

In Fig. 5(a), the black (ILP and ILR2) and red (ILR1) lines help to interpret the data. In the first section, from 0 to 8/14 nm in base length, the linear increase of the QD height is shown, where the QDs were cleaved at their edge and their cross section is close

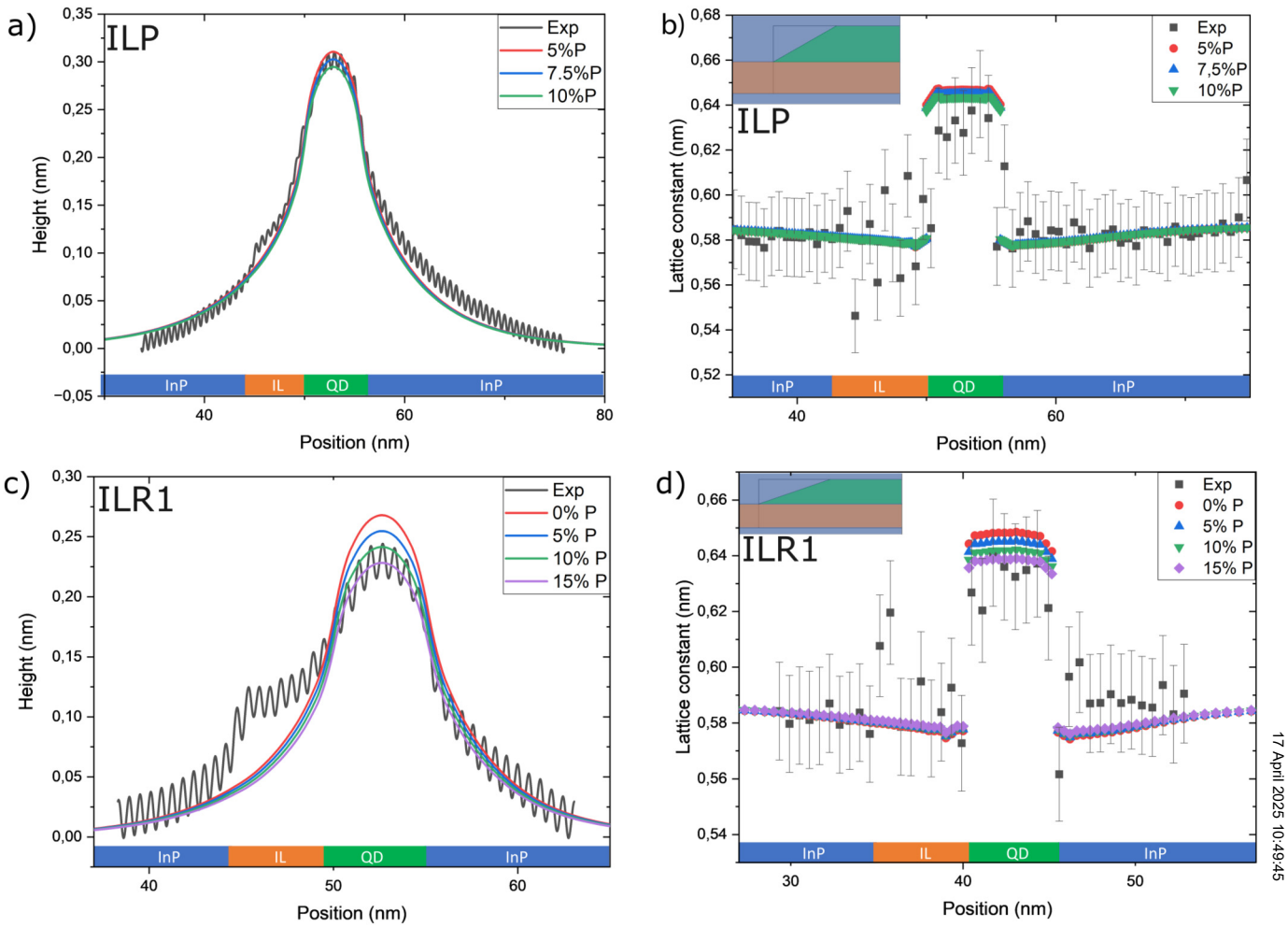

FIG. 6. (a) X-STM height profile taken on at the center of the ILP QD in Fig. 3(a) together with calculated relaxation profiles with varying P concentrations from the FES. (b) Experimental lattice constant profile obtained from the same line profile as of (a) is shown with a calculated lattice constant from FES. (c) Plot of the height profile taken on the ILR1 QD in Fig. 4(a) and plots of the relaxation profiles from the FES. (d) Experimental lattice constant obtained from the same line profile as of (c) and FES results. The insets in the top left corner in (b) and (d) show the details of the geometry used for the simulations.

to a triangle. The plateaus, starting approximately for the black line at 8 nm and for the red one at 14 nm, represent the mean height of the QDs derived from the graphs in Figs. 5(c) and 5(e) for the black line and Fig. 5(d) for the red one. These QDs were cleaved closer to their core and, therefore, showed a trapezoidal cross section. Red and black data points (ILR1 and ILR2) show good agreement with the QD model of a truncated pyramid with sides aligned to the (010) directions, proposed in Bruls *et al.*[30] The blue data points (ILP) also follow this QD model but with a component of few taller QDs (with a height larger than 5 nm).

In Fig. 5(b), the top length against the base length is plotted for all the measured QDs. The black and red lines in the graph have a slope equal to 1 since a 1 nm increase in the top length corresponds to a 1 nm increase in the base length as can be seen by the inset of Fig. 5(b). The intercept, however, represents the length of the base where the flat top starts to appear. It is also shown in Fig. 5(a) as the position where the QD line reaches the plateau. All three data sets follow a linear trend as it is expected for a pyramidal dot shape, where the quantum dot is aligned with its diagonals in the [110] and [$\bar{1}$10] directions.[15]

The graphs [(c)–(e)] of Fig. 5 depict the distribution of the QD height measured in bilayers. Figure 5(c) shows a distribution with a mean height value of 5.1 $\pm$ 0.2 bilayers for the sample ILP. Figure 5(d) shows for ILR1 a distribution with fewer dots but with a higher mean height value of 7.4 $\pm$ 0.2 bilayers. The last case, ILR2, Fig. 5(e) shows a mean height value of 4.5 $\pm$ 0.1 bilayers. The height distribution of the three QD layers differs not only per IL but also per amount of In deposited (see sec. II). The ILR1 QD layer has

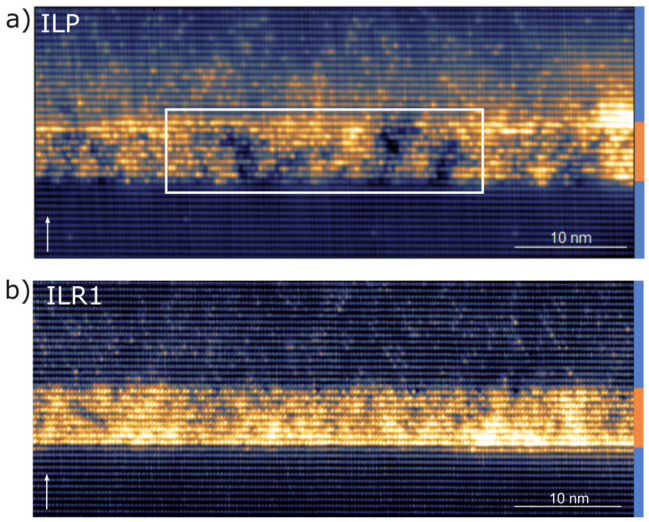

FIG. 7. (a) 53 × 22 nm^2 X-STM filled states image taken at −2.8 V and 100 pA of the InGaAsP IL of ILP. The contrast scale ranges from 22 (dark) to 104 pm (bright). The region represented is the InGaAsP IL of ILP. Lateral composition modulation is visible through the darker and brighter regions highlighted by the rectangle. (b) 56 × 22 nm^2 filled state X-STM image taken at −3 V and 100 pA of the InGaAs IL of ILR1; the contrast scale ranges from 22 (dark) to 104 pm (bright). Some lateral composition modulation is present, in particular, in the bottom right area with a bright region and on the left with some darker regions.

the least amount of In deposited; yet, it shows the distribution with the largest mean height value. ILP and ILR2 have comparable amounts of In deposited and similar height distributions.

There is a noticeable difference in the average height scaled in the bilayer corresponding to varying amounts of deposited In. Surfaces with less In deposited exhibit higher average height values. This behavior may initially appear counter-intuitive, as one might expect that a greater amount of material would lead to larger and taller QDs. However, we propose the following growth mechanism at play. During the deposition process, as In is supplied to the surface, a finite number of In atoms bind to each other to form nucleation clusters on the IL, where they subsequently coalesce into larger In droplets. Once the desired In deposition is achieved, the In flux is halted, and approximately 1 min later, the surface is supplied with As to crystallize the QDs.[24] A key factor to consider is the number of nucleation clusters on the surface, which varies depending on the amount of In supplied.[34] When a smaller amount of In is provided, fewer nucleation sites are formed, resulting in a greater average distance between them compared to a sample where twice as much In was supplied, leading to twice as many nucleation sites.[34] The increased distance between nucleation sites allows for a larger area around each nucleation site for In droplets to accumulate mobile indium atoms on the surface, consequently leading to the formation of fewer, larger, and taller dots. Conversely, when a larger amount of In is supplied, more nucleation sites are formed, thereby increasing their density and reducing the area available for material accumulation around each nucleation site. Consequently, this results in the formation of QDs with a smaller area and a shorter height.

4. Composition analysis

To study the internal composition of the QDs reported in Figs. 3(a) (ILP) and 4(a) (ILR1), we performed finite element simulations of the X-STM measured height profiles and the lattice constant. The relaxation profiles are taken from X-STM images measured at a large negative bias, such as shown in Fig. 4(a), minimizing the contribution from electronic states, and the topographic contrast is mainly determined by the outward relaxation. The lattice constant profiles are measured from the relaxation profiles by determining the position of each atomic row and calculating the distance between each one of them. The profiles and FES results are shown in Figs. 6(a) and 6(b) for ILP and 6(c) and 6(d) for ILR1. Figures 6(a) and 6(c) both show an outward surface relaxation. Upon cleaving, the compressively strained QD, due to the 3% lattice mismatch between the InAs (0.606 nm) of the QD and InP (0.587 nm) of the host, is free to relax.[30,35] Fitting the described relaxation and the lattice constant profile with those obtained by the FES gives us insight into the QD composition. The simulations carried out in this work follow the same procedure as in Ref. 15.

The geometrical models used in the FES for the rhomboid QDs are shown in the inset of Figs. 6(b) and 6(d). We selected one of the largest dots in the measurements as we expected that those were cleaved through their center. Due to the asymmetry in the rhomboid base and the different cleaving orientations [the inset of Fig. 5(a)], the two QDs have different relaxation profiles (max height for ILP 0.30 nm and for ILR1 0.25 nm) due to the different amount of material still embedded below the surface. After this difference was included in the geometrical model, the last free fitting parameter is the internal composition.

Figure 6(a) shows the height profile for a QD in the ILP sample. The optimal agreement between the FES and the observed relaxation is reached for a P concentration of about 7.5%. The lattice constant profile in Fig. 6(b) does not exclude any simulation results in the simulated range of P concentrations as all the simulations profiles are within the error bar of the experimental data. However, looking at the X-STM image in Fig. 3(a), it is clear that the P composition (dark atomic-sized depressions in the QD core contrast) is well below 7.5% as the QD core contrast is very uniform, with some minor fluctuations only in the left side. Therefore, for the ILP QD, we can estimate that the group V composition is comprised of at least 95% As and less than 5% P.

For ILR1, in Fig. 6(c), the best agreement is reached with a P concentration of 15%. The lattice constant simulation in Fig. 6(d) does not exclude any of the simulated values, although 15% seems to fit better the experimental result. Comparing these results to the X-STM measurement of Fig. 4(a), we can exclude a P incorporation higher than 10%. We, thus, estimate for an ILR1 QD a group V composition comprised of at least 90% As and less than 10% P.

For both the ILP and ILR1/2 QDs, we found a low amount P intermixing, which is very similar to those grown directly on InP.[15] In all cases, we can consider these droplet epitaxy QDs dots as having a nearly pure InAs composition, which is very different

from Stranski–Krastanov QDs that typically show strong (In/Ga)As intermixing and internal composition gradients.[25,36,37]

In the ILR1 case, the IL region below the QDs (lattice matched to InP, see Sec. II) is not well fitted by our FES relaxation profile in Fig. 6(c). We ascribe this difference to a remaining electronic contrast contribution that was not completely suppressed due to the different material compositions of the IL region from the host. In the ILP case instead, we can observe a larger variation in the lattice constant profile in the IL region. This is related to composition fluctuations in the IL quaternary alloy.

The relaxation profiles are also influenced by group III composition, and thus, Ga intermixing can contribute to the relaxation profiles and the lattice constant profile. In the SM, two images taken at negative and positive biases of the same ILP QDs are shown and no Ga intermixing is observed. Since the X-STM sample measurements were taken under a negative bias imaging the group V sublattice, any contrast fluctuation in the X-STM images is mainly due to variations in the As and P concentrations. The group III purity of DE QDs is known to be higher when compared to Stranski–Krastanov QDs.[35,38]

Comparing these results to the QDs grown directly on InP, shown in Figs. 3, 4, and 6 of Ref. 15, we can see that ILR1 and ILR2 QDs tend to incorporate somewhat more P than QDs grown directly on InP, a conclusion qualitatively reached in Ref. 15. X-STM images of ILP QDs (Fig. 3) are very similar to QDs directly grown on InP reported in Ref. 15 with a similar high purity level. The IL presence in ILP allows us to prevent both etch pits and trenching mechanisms. It has been demonstrated that QDs with etch pits underneath their base can reduce the finite structure splitting (FSS) of the QDs,[25,39] although only when found at specific positions. However, currently, we do not have control over the position of such etch pits in InP and their origin is not yet well-understood. In this study, we have shown that the growth of ILP QDs does not lead to etch pits and hence, a source of uncontrolled influence on FSS in high-quality QDs relevant to quantum telecommunications and photonics is removed.

C. Lateral composition modulation

X-STM images, such as those reported in Figs. 7(a) and 7(b), show the IL region for ILP and ILR1 with a normalized contrast scale allowing for comparison. In both cases, the IL region is lattice-matched to the InP above and below, as can be seen in the lattice constant profiles [Figs. 6(b)–6(d)]. The generally brighter contrast seen in the IL regions is not due to strain relaxation but rather to a difference in the bandgap between InP and InGaAsP. The observed local contrast variation in the IL is attributed to local composition fluctuations caused by the random distribution of chemical elements within the IL. These local variations can be enhanced by local composition modulation (LCM) induced by partial phase separation of the alloy. For example, this could result in GaAs or InAs-rich areas in InGaAs, or InAs and GaP-rich areas in InGaAsP.[40] The local composition fluctuations affect the STM contrast by causing local strain modulation (inducing topographic height variations) and local bandgap variation (causing electronic-related height variations). A limiting case for LCM is reached when nanostructures, such as quantum dots (QDs), form due to strong or complete phase separation, as reported in Ref. 41.

Comparing the IL region of ILR1/2 to that in ILP, as presented in Fig. 7, immediately reveals a different contrast picture. We observe much stronger contrast variations in ILP compared to ILR1, as demonstrated by the darker and brighter regions within the white rectangle. We attribute this stronger contrast variation in the X-STM images obtained on ILP to LCM. LCM in the form of filamentation has been clearly shown in X-STM studies of multilayered quantum wells of InGaAs and InAlAs.[40,42–44] In these studies, the lateral contrast variations observed in the quantum well material exhibit similar behavior to what we observe here. We, thus, confirm what was previously suggested in Sala *et al.*,[24] where the LCM presence for the InGaAsP was theorized. The visible filamentation in those samples was due to partial phase separation in the two superlattice materials, combined with strain-induced nucleation that extends local composition variations in the growth direction. In the quaternary (InGaAsP) material of the IL used in ILP, the LCM forms directly during the growth of the IL. Although generally LCM might be detrimental for lasing applications,[45] our QDs on both ILs have shown very good optical quality,[23,24] and they do not appear to be degraded by the LCM. Throughout our investigation, LCM was observed in various images for ILP, but no correlation with the QD formation was found.

IV. CONCLUSIONS

We studied InAs droplet epitaxy quantum dots grown by MOVPE on InGaAsP and on InGaAs interlayers lattice-matched to InP by means of AFM, X-STM, and FES. In the current work, we show that the introduction of P in the interlayer region, as part of the quaternary material InGaAsP, effectively suppresses the etch pits or trenches. By studying post-cleavage relaxation profiles and lattice constant profiles, we found that the growth on InGaAsP enhances the purity of the QDs compared to the same growth on InGaAs, producing almost pure dots. Comparing growth on InGaAsP to the growth on InP, it showed high-quality QDs with similar uniformity in the QD core and the absence of etching and trenching effects. As previously suggested in Sala *et al.*,[24] we confirmed the presence of atomic scale lateral composition modulation due to partial phase separation of GaP and InAs, in the InGaAsP interlayer. The MOVPE-grown layers showed a high crystal quality with no observable dislocations or defects. Therefore, we conclude that InAs droplet dots grown on InGaAsP show excellent prospects to open up an avenue for applications in optical communication and opto-electronic devices.

SUPPLEMENTARY MATERIAL

See the supplementary material for (1) the untreated plots of the QD top length against the base length and the QD height against the base length. (2) an X-STM bias flip image of the ILP sample (−1.9 to 2 V) showing the corrugation shift of the surface due to the voltage bias-induced change in the observed sublattice, allowing the determination of the surface plane. (3) X-STM negative and positive bias images of the same QDs that show no internal contrast variation in the positive bias, which suggests no Ga intermixing and overall high purity of the QDs.

ACKNOWLEDGMENTS

We thank the Nederlandse Organisatie voor Wetenschappelijk onderzoek (NWO) for funding this research through the Zwaartekracht project on Integrated Nanophotonics with Project No. 10018478. We would also like to acknowledge the support by EPSRC (UK Engineering and Physical Sciences Research Council) (Grant No. EP/R03480X/1) (Hetero-print: scalable manufacturing technology) and EP/T001011/1 (Quantum Communication Hub). Finally, we thank the support of the UKRI (UK Research and Innovation) Project No. 48484 (Qfoundry).

AUTHOR DECLARATIONS

Conflict of Interest

The authors have no conflicts to disclose.

Author Contributions

E.G.B. and R.S.R.G. performed the X-STM measurements, E.M.S. designed and grew the samples by MOVPE, E.G.B. wrote the manuscript, and all the authors contributed to its editing. P.M.K. and J.H. provided overall supervision. All the authors have approved the final version of the manuscript. We acknowledge Dr. Young In Na for the AFM measurements.

E. G. Banfi: Conceptualization (equal); Data curation (equal); Formal analysis (equal); Investigation (equal); Resources (equal); Writing – original draft (lead); Writing – review & editing (equal). **E. M. Sala:** Conceptualization (equal); Data curation (equal); Formal analysis (equal); Investigation (equal); Methodology (equal); Resources (equal); Writing – original draft (supporting); Writing – review & editing (equal). **R. S. R. Gajjela:** Investigation (equal); Writing – review & editing (supporting). **J. Heffernan:** Conceptualization (equal); Funding acquisition (equal); Project administration (equal); Supervision (supporting); Writing – review & editing (supporting). **P. M. Koenraad:** Conceptualization (equal); Funding acquisition (equal); Project administration (equal); Supervision (lead); Writing – review & editing (equal).

DATA AVAILABILITY

The data that support the findings of this study are available from the corresponding author upon reasonable request.

REFERENCES

[1]L. E. Brus, J. Chem. Phys. **79**, 5566 (1983).
[2]N. N. Ledentsov, Semicond. Sci. Technol. **26**, 014001 (2010).
[3]D. Bimberg, M. Grundmann, F. Heinrichsdorff, N. Ledentsov, V. Ustinov, A. Zhukov, A. Kovsh, M. Maximov, Y. Shernyakov, B. Volovik, A. Tsatsul'nikov, P. Kop'ev, and Z. Alferov, Thin Solid Films **367**, 235 (2000).
[4]*Quantum Dots for Quantum Information Technologies*, Nano-Optics and Nanophotonics, edited by P. Michler (Springer, Cham, 2017), see https://link.springer.com/book/10.1007/978-3-319-56378-7.
[5]T. Müller, J. Skiba-Szymanska, A. B. Krysa, J. Huwer, M. Felle, M. Anderson, R. M. Stevenson, J. Heffernan, D. A. Ritchie, and A. J. Shields, Nat. Commun. **9**, 862 (2018).
[6]M. Anderson, T. Müller, J. Huwer, J. Skiba-Szymanska, A. B. Krysa, R. M. Stevenson, J. Heffernan, D. A. Ritchie, and A. J. Shields, npj Quantum Inf. **6**, 14 (2020).
[7]J. Skiba-Szymanska, R. M. Stevenson, C. Varnava, M. Felle, J. Huwer, T. Müller, A. J. Bennett, J. P. Lee, I. Farrer, A. B. Krysa, P. Spencer, L. E. Goff, D. A. Ritchie, J. Heffernan, and A. J. Shields, Phys. Rev. Appl. **8**, 014013 (2017).
[8]A. Marent, T. Nowozin, M. Geller, and D. Bimberg, Semicond. Sci. Technol. **26**, 014026 (2010).
[9]E. M. Sala, I. F. Arikan, L. Bonato, F. Bertram, P. Veit, J. Christen, A. Strittmatter, and D. Bimberg, Phys. Status Solidi (b) **255**, 1800182 (2018).
[10]S. Anantathanasarn, R. Nötzel, P. J. van Veldhoven, F. W. M. van Otten, Y. Barbarin, G. Servanton, T. de Vries, E. Smalbrugge, E. J. Geluk, T. J. Eijkemans, E. A. J. M. Bente, Y. S. Oei, M. K. Smit, and J. H. Wolter, Appl. Phys. Lett. **89**, 073115 (2006).
[11]Z. Liu, C.-H. Lin, B.-R. Hyun, C.-W. Sher, Z. Lv, B. Luo, F. Jiang, T. Wu, C.-H. Ho, H.-C. Kuo, and J.-H. He, Light: Sci. Appl. **9**, 83 (2020).
[12]O. E. Semonin, J. M. Luther, and M. C. Beard, Mater. Today **15**, 508 (2012).
[13]S. Y. Madani, F. Shabani, M. V. Dwek, and A. M. Seifalian, Int. J. Nanomed. **8**, 941 (2013).
[14]T. Heindel, J.-H. Kim, N. Gregersen, A. Rastelli, and S. Reitzenstein, Adv. Opt. Photonics **15**, 613 (2023).
[15]R. S. R. Gajjela, E. M. Sala, J. Heffernan, and P. M. Koenraad, ACS Appl. Nano Mater. **5**, 8070 (2022).
[16]T. Sadeev, D. Arsenijević, and D. Bimberg, Appl. Phys. Lett. **109**, 161104 (2016).
[17]M. Razeghi, Nature **369**, 631 (1994).
[18]P. Holewa, M. Gawełczyk, C. Ciostek, P. Wyborski, S. Kadkhodazadeh, E. Semenova, and M. Syperek, Phys. Rev. B **101**, 195304 (2020).
[19]M. Anderson, T. Müller, J. Skiba-Szymanska, A. B. Krysa, J. Huwer, R. M. Stevenson, J. Heffernan, D. A. Ritchie, and A. J. Shields, Appl. Phys. Lett. **118**, 014003 (2021).
[20]C. L. Phillips, A. J. Brash, M. Godsland, N. J. Martin, A. Foster, A. Tomlinson, R. Dost, N. Babazadeh, E. M. Sala, L. Wilson, J. Heffernan, M. S. Skolnick, and A. M. Fox, Sci. Rep. **14**, 4450 (2024).
[21]E. M. Sala, Y. I. Na, M. Godsland, A. Trapalis, and J. Heffernan, Phys. Status Solidi (RRL) **14**, 2000173 (2020).
[22]E. M. Sala, M. Godsland, A. Trapalis, and J. Heffernan, Phys. Status Solidi (RRL) **15**, 2100283 (2021).
[23]E. M. Sala, M. Godsland, Y. I. Na, A. Trapalis, and J. Heffernan, Nanotechnology **33**, 065601 (2021).
[24]E. M. Sala, Y. I. Na, M. Godsland, and J. Heffernan, Phys. Status Solidi (RRL) **18**, 2300340 (2024).
[25]R. S. R. Gajjela, N. R. S. Van Venrooij, A. R. Da Cruz, J. Skiba-Szymanska, R. M. Stevenson, A. J. Shields, C. E. Pryor, and P. M. Koenraad, Nanotechnology **33**, 305705 (2022).
[26]D. Fuster, K. Abderrafi, B. Alén, Y. González, L. Wewior, and L. González, J. Cryst. Growth **434**, 81 (2016).
[27]A. Ponchet, L. Pedesseau, A. Le Corre, C. Cornet, and N. Bertru, Appl. Phys. Lett. **114**, 173102 (2019).
[28]Q. Gong, P. Offermans, R. Nötzel, P. M. Koenraad, and J. H. Wolter, Appl. Phys. Lett. **85**, 5697 (2004).
[29]S. Hasan, C. Merckling, M. Pantouvaki, J. Meersschaut, J. Van Campenhout, and W. Vandervorst, J. Cryst. Growth **509**, 133 (2019).
[30]D. Bruls, J. Vugs, P. Koenraad, M. Skolnick, M. Hopkinson, and J. Wolter, Appl. Phys. A **72**, S205 (2001).
[31]A. Michon, I. Sagnes, G. Patriarche, G. Beaudoin, M. N. Mérat-Combes, and G. Saint-Girons, Phys. Rev. B **73**, 165321 (2006).
[32]R. M. Feenstra, J. A. Stroscio, J. Tersoff, and A. P. Fein, Phys. Rev. Lett. **58**, 1192 (1987).

[33]D. M. Bruls, J. W. A. M. Vugs, P. M. Koenraad, H. W. M. Salemink, J. H. Wolter, M. Hopkinson, M. S. Skolnick, F. Long, and S. P. A. Gill, Appl. Phys. Lett. **81**, 1708 (2002).
[34]C. Heyn, A. Stemmann, A. Schramm, H. Welsch, W. Hansen, and Á. Nemcsics, Phys. Rev. B **76**, 075317 (2007).
[35]P. Offermans, P. M. Koenraad, J. H. Wolter, K. Pierz, M. Roy, and P. A. Maksym, Phys. Rev. B **72**, 165332 (2005).
[36]P. Offermans, P. M. Koenraad, J. H. Wolter, K. Pierz, M. Roy, and P. A. Maksym, Phys. E: Low-Dimens. Syst. Nanostruct. **26**, 236 (2005). International Conference on Quantum Dots.
[37]A. Lenz, R. Timm, H. Eisele, C. Hennig, S. K. Becker, R. L. Sellin, U. W. Pohl, D. Bimberg, and M. Dähne, Appl. Phys. Lett. **81**, 5150 (2002).
[38]N. Liu, J. Tersoff, O. Baklenov, A. L. Holmes, and C. K. Shih, Phys. Rev. Lett. **84**, 334 (2000).
[39]N. R. S. van Venrooij, A. R. da Cruz, R. S. R. Gajjela, P. M. Koenraad, C. E. Pryor, and M. E. Flatté, Phys. Rev. B **109**, L201405 (2024).
[40]R. R. LaPierre, T. Okada, B. J. Robinson, D. A. Thompson, and G. C. Weatherly, J. Cryst. Growth **158**, 6 (1996).
[41]J. He, R. Nötzel, P. Offermans, P. M. Koenraad, Q. Gong, G. J. Hamhuis, T. J. Eijkemans, and J. H. Wolter, Appl. Phys. Lett. **85**, 2771 (2004).
[42]C. K. W. Wyllie and D. A. Thompson, Semicond. Sci. Technol. **13**, 750 (1998).
[43]T. L. McDevitt, S. Mahajan, D. E. Laughlin, W. A. Bonner, and V. G. Keramidas, Phys. Rev. B **45**, 6614 (1992).
[44]P. Offermans, P. M. Koenraad, J. H. Wolter, J. D. Song, J. M. Kim, S. J. Bae, and Y. T. Lee, Appl. Phys. Lett. **82**, 1191 (2003).
[45]J. M. Chauveau, A. Trampert, M. A. Pinault, E. Tournié, K. Du, and K. H. Ploog, J. Cryst. Growth **251**, 383 (2003).